Materials Advances

ROYAL SOCIETY OF CHEMISTRY

PAPER

View Article Online
View Journal | View Issue

Cite this: *Mater. Adv.*, 2024, 5, 2934

Europium-doped hybrid nano-complexes: a potential strategy for metastasis prevention in osteosarcoma†

Yu-Chi Wang, ‡[a] Fu-I Tung, ‡[bc] Zheng-Ying Sung, [a] Mei-Hsiu Chen, [de] Ming-Hong Chen [fg] and Tse-Ying Liu *[a]

Received 31st October 2023,
Accepted 15th February 2024

DOI: 10.1039/d3ma00939d

rsc.li/materials-advances

Metastasis is a major issue in cancer therapy, resulting in poor prognosis and death. However, there is currently no widely established prophylactic strategy for early metastasis in the clinical setting. Although water-soluble $EuCl_3 \cdot 6H_2O$ has the potential to exhibit a metastasis-inhibiting effect similar to migrastatics and matrix metalloproteinase inhibitors (MMPIs), intravenous administration of europium (Eu)-containing compound solution may not efficiently accumulate Eu ions in tumors and could be rapidly cleared from the body. In this study, we developed Eu ion-doped superparamagnetic iron oxides incorporated into bovine serum albumin hybrid nano-complexes (Eu:SPIO@BSA nano-complexes) to enhance tumor accumulation and prevent metastatic osteosarcoma *via* intravenous administration. *In vitro* studies showed that Eu:SPIO@BSA nano-complexes had a migration-inhibiting effect and affected pseudopodia formation in K7M2 cells. *In vivo* studies showed that distant lung metastasis was inhibited by the magnetism-enhanced targeted delivery of Eu:SPIO@BSA nano-complexes. Taken together, our results provide evidences that the Eu:SPIO@BSA nano-complex, with precise delivery, higher hemocompatibility and low liver toxicity, is a potential candidate for improving the therapeutic efficacy of metastasis prevention in osteosarcoma.

1. Introduction

Metastasis is a critical factor contributing to treatment failure in cancer patients.[1] Approximately 90% of patients receiving standard treatments eventually die due to metastasis, as tumor spread is often unpredictable.[2,3] To date, there is no widely established prophylactic strategy for early metastasis in the clinical setting. Current medicines for metastasis treatment still focus on tumor shrinkage and proliferation control; however, they cannot prevent the occurrence of metastasis completely.[4] In particular, osteosarcoma presents a notable case with a less than 30% five-year survival rate, primarily attributed to distant lung metastasis.[5,6] Despite patients receiving surgery combined with adjuvant radiotherapy and chemotherapy in the early stage, the outcomes were not satisfactory. Therefore, it is essential to develop new therapeutic agents to inhibit the initial tumor metastasis.

The metastasis cascade involves several processes, including migration, invasion, intravasation, extravasation, and colonization of secondary tumors.[7] Among these processes, tumor cell migration and invasion play pivotal roles in the early spread of tumors from the primary sites. Consequently, several studies have proposed anti-metastatic agents, such as migrastatics (*i.e.*, anti-migration drugs)[8] or matrix metalloproteinase inhibitors (MMPIs),[9] to intervene in the occurrence of initial metastasis. Notably, lanthanides, including europium (Eu) ions, have shown potential in exhibiting effects similar to migrastatics and MMPIs,[10,11] with Eu ions demonstrating particularly promising inhibitory efficacy.[12] However, our preliminary study suggests that the use of Eu ions dissociated from water-soluble Eu-containing compounds, administered *via* the intravenous route, may present challenges due to their poor tumor-targeting nature and potential hemocompatibility issues. This indicates the need for cautious consideration when exploring Eu ions as

[a] *Department of Biomedical Engineering, National Yang Ming Chiao Tung University, Taipei 112304, Taiwan. E-mail: tyliu5@nycu.edu.tw*
[b] *Department of Orthopaedics, Yang-Ming branch, Taipei City Hospital, Taipei 111024, Taiwan*
[c] *Department of Health and Welfare, College of City Management, University of Taipei, Taipei 111036, Taiwan*
[d] *Department of Internal Medicine, Far Eastern Memorial Hospital, New Taipei City 220216, Taiwan*
[e] *Department of Biomedical Engineering, Ming Chuang University, Taoyuan 333, Taiwan*
[f] *Division of Neurosurgery, Department of Surgery, Far Eastern Memorial Hospital, New Taipei City 220216, Taiwan*
[g] *Department of Electrical Engineering, Yuan Ze University, Taoyuan City 320315, Taiwan*

† Electronic supplementary information (ESI) available. See DOI: https://doi.org/10.1039/d3ma00939d

‡ These authors contributed equally to this work.

a potential anti-metastatic agent. Further research is required to develop a suitable dosage form for delivering Eu ions that ensures targeted delivery and minimizes any potential toxicity concerns. In our previous study, we developed and employed Eu-doped CaF_2 nanoparticles as an intraosseous implant, in which the Eu-containing implant demonstrated a metastasis-inhibiting effect in *in vivo* experiments.[13] In this current study, we proposed an intravenous (I.V.) formulation as an alternative strategy utilizing Eu-doped hybrid nano-complexes as migrastatics and MMPIs. The main objective is to address diverse clinical conditions, especially for the early stage of osteosarcoma where resection is not feasible.

To precisely deliver the migration/invasion-inhibiting effect of Eu ions to the tumor tissue and cells, we developed a nanovehicle in which Eu was doped into superparamagnetic iron oxides (SPIO). The resulting nanocrystals (*i.e.*, Eu:SPIO) were incorporated into bovine serum albumin (BSA) to prepare new hybrid nano-complexes, hereinafter referred to as Eu:SPIO@BSA nano-complexes. This approach utilized the well-recognized magnetic guidance properties of SPIO at the nanoscale,[14,15] enabling precise delivery of the Eu:SPIO nanocrystals through magnetic attraction. Furthermore, BSA with high affinity to tumor cells facilitated enhanced permeability and retention (EPR) and active targeting.[16] These properties were leveraged when incorporating Eu:SPIO nanocrystals into BSA, further augmenting both passive and active targeting. Currently, the combination of SPIO and BSA has been used as an agent for targeted imaging;[17,18] however, similar vehicles have rarely been reported for metastasis inhibition. Moreover, some studies have indicated that current medicines that directly inhibit tumor cell proliferation may interfere with the assessment of preventive metastasis.[8,19] In contrast, the proposed vehicle in this study, Eu:SPIO@BSA nano-complexes, demonstrated limited toxicity for tumor cells, making it suitable for evaluating the therapeutic efficacy of metastasis inhibition.

In this study, our objective was to prepare Eu:SPIO@BSA nano-complexes and evaluate their inhibitory efficacy on metastasis, with a particular focus on lung metastasis of osteosarcoma. This aspect of osteosarcoma holds significant implications for patient prognosis and treatment outcomes. Through a series of *in vitro* and *in vivo* experiments, including scratch-wound healing assays, transwell assays, and animal experiments, we assessed the potential of Eu:SPIO@BSA nano-complexes, using $EuCl_3{\cdot}6H_2O$ as the comparison group, in preventing metastasis. The utilization of Eu:SPIO@BSA nano-complexes as a targeted delivery system holds promise in enhancing the precision and effectiveness of anti-metastatic therapies. This innovative approach could be combined with standard cancer treatments in the future, revolutionizing the field of cancer treatment.

2. Experimental methods

2.1 Materials preparation

Iron(III) acetylacetonate (97%) and Eu(III) acetate hydrate were obtained from Alfa Aesar. 1,2-Hexadecanediol was obtained from TCI. Oleic acid, benzyl ether (98%), BSA, and BSA conjugated fluorescein isothiocyanate (FITC) were obtained from Sigma Aldrich. Oleylamine was obtained from ACROS. Dichloromethane (DCM 99.9%) was obtained from ECHO Chemical.

2.1.1 Synthesis of hydrophobic SPIO and Eu:SPIO nanocrystals. Hydrophobic SPIO and Eu-doped SPIO (*i.e.*, Eu:SPIO) nanocrystals were synthesized *via* pyrolysis.[20] In brief, iron(III) acetylacetonate (1 mmol), 1,2-hexadecanediol (10 mmol), oleic acid (3.2 mmol), and oleylamine (3.2 mmol) were mixed with 10 mL benzyl ether in a 100 mL three-neck bottle. The mixture was stirred at 125 °C for 30 min under an argon flow to remove water and oxygen, then heated to 210 °C for 1 h, and refluxed at 315 °C for 20 min. After cooling to room temperature, the black-brown mixture was collected by centrifugation at 13 200 rpm for 10 min and then washed three times with excess ethanol to remove the solvent. The SPIO nanocrystals were collected and redispersed in *n*-hexane.

Eu:SPIO nanocrystals were prepared using the following procedure: briefly, iron(III) acetylacetonate (2 mmol), europium(III) acetate hydrate (1.2 mmol), 1,2-hexadecanediol (16 mmol), oleic acid (8.98 mmol), and oleylamine (8.93 mmol) were mixed with 30 mL benzyl ether in a 100 mL three-neck bottle. The mixture was stirred at 125 °C for 20 min under an argon flow to remove water and oxygen, and then heated to 205 °C for 1 h, and subsequently refluxed at 320 °C for 20 min. After cooling to room temperature, the black-brown mixture was collected by centrifugation at 10 000 rpm for 10 min and then washed three times with excess ethanol to remove the solvent. The Eu:SPIO nanocrystals were collected and redispersed in *n*-hexane.

2.1.2 Preparation of SPIO@BSA and Eu:SPIO@BSA nano-complexes. Hydrophilic SPIO@BSA and Eu:SPIO@BSA nano-complexes were prepared using emulsification and coacervation methods.[21] In brief, hydrophobic SPIO and Eu:SPIO nanocrystals (35 mg) were dispersed in DCM and added to 5 mL 4% BSA solution. The ratio of DCM containing hydrophobic SPIO and Eu : SPIO nanocrystals to 4% BSA solution was 1 : 20. The mixture was then homogenized for 5 min on ice. After homogenization, 99% ethanol was added into the mixture dropwise at a rate of 4 mL min^{-1} using a peristaltic pump. When the solution became turbid, it was stirred at room temperature for 30 min in a hood. Finally, the obtained products (SPIO@BSA and Eu:SPIO@BSA nano-complexes) were washed several times with ethanol and deionized water and lyophilized for long-term storage.

2.1.3 Preparation of SPIO@FITC-BSA and Eu:SPIO@FITC-BSA fluorescence nano-complexes. The preparation method was the same as that of the SPIO@BSA and Eu:SPIO@BSA nano-complexes. However, the BSA solution was replaced with BSA-conjugated FITC.

2.1.4 Characterization of SPIO@BSA and Eu:SPIO@BSA nano-complexes. The crystal structure and elemental composition of the SPIO and Eu:SPIO nanocrystals were characterized using X-ray diffraction (XRD; Bruker, D2 Phaser) and X-ray photoelectron spectroscopy (XPS; Thermo Scientific, Theta Probe), respectively. XPS spectra were analyzed using CasaXPS software. The morphologies of the SPIO and Eu:SPIO nanocrystals,

SPIO@BSA, and Eu:SPIO@BSA nano-complexes were observed using transmission electron microscopy (TEM; JEOL, JEM-2000EXII). Amount of BSA, and magnetic properties of SPIO@BSA and Eu:SPIO@BSA nano-complexes were characterized using thermogravimetric analysis (TGA; Mettler-Toledo, 2-HT), and SQUID (Quantum Design North America), respectively. ICP-MS (Thermo-Element XR) analysis was performed to determine the amounts of Fe and Eu in the SPIO nanocrystals, Eu:SPIO nanocrystals, SPIO@BSA nano-complexes, and Eu:SPIO@BSA nano-complexes.

2.2 Cell culture

The osteoblastic cell line (MC3T3-E1) and the mouse osteosarcoma cell line (K7M2) were obtained from the Bioresource Collection and Research Center (Taiwan). The MC3T3-E1 and K7M2 cells were cultured in α-minimal essential medium (α-MEM) and Dulbecco's modified Eagle's medium (DMEM), respectively, with 10% fetal bovine serum (FBS) and 1% penicillin–streptomycin (PS) in a 5% CO_2 incubator at 37 °C. The medium was renewed every 2 or 3 days, and cells were passaged once 80% confluence was reached.

2.2.1 Cellular internalization. MC3T3-E1 and K7M2 cells were seeded onto 18 mm glass slides in 12-well culture plates at a density of 1×10^5 cells per well. SPIO@FITC-BSA and Eu:SPIO@FITC-BSA nano-complexes (400 μg mL^{-1}) were incubated with cells for 24 h. After washing with PBS, cells were stained with Fluoroshield™ DAPI (GeneTex) and Alexa Fluor 568 conjugated phalloidin (Invitrogen™). The localization of SPIO@FITC-BSA and Eu:SPIO@FITC-BSA nano-complexes was observed using confocal laser microscopy (CLSM, ZEISS, LSM880).

2.2.2 Scratch wound-healing assay. The cell migration ability was assessed using a scratch wound-healing assay. K7M2 cells were seeded in 6-well culture plates at a density of 5×10^5 cells per well for 24 h. The cells were then incubated with or without samples (*i.e.*, SPIO@BSA nano-complexes, Eu:SPIO@BSA nano-complexes, and $EuCl_3{\cdot}6H_2O$) for 24 h. The concentrations of SPIO@BSA, Eu:SPIO@BSA nano-complexes, and $EuCl_3{\cdot}6H_2O$ were 715 μg mL^{-1}, 530 μg mL^{-1}, and 18 μg mL^{-1}, respectively. The concentrations of SPIO@BSA and Eu:SPIO@BSA nano-complexes with the similar Fe content were selected. In addition, Eu:SPIO@BSA nano-complexes and $EuCl_3{\cdot}6H_2O$ with the similar Eu content were selected. After 24 h of treatment, the cells were scratched using a 1 mL pipette tip to create a scratch wound and then allowed to migrate for 24–48 h. The experiments were performed three times for each group, and the cell migration was measured using a phase-contrast microscope (Nikon, TE2000-U). The wound closure ratio of cell migration for each image was normalized according to the initial scraped area using the ImageJ software.

2.2.3 Transwell migration/invasion assay. Cell migration and invasion abilities were detected using a transwell migration assay. K7M2 cells were seeded in 6-well culture plates at a density of 5×10^5 cells per well for 24 h. The cells were then incubated with or without samples (*i.e.*, SPIO@BSA nano-complexes, Eu:SPIO@BSA nano-complexes, and $EuCl_3{\cdot}6H_2O$) for 24 h. The concentrations of SPIO@BSA nano-complexes, Eu:SPIO@BSA nano-complexes, and $EuCl_3{\cdot}6H_2O$ were 715 μg mL^{-1}, 530 μg mL^{-1}, and 18 μg mL^{-1}, respectively. The concentrations of SPIO@BSA and Eu:SPIO@BSA nano-complexes with the similar Fe content were selected. In addition, Eu:SPIO@BSA nano-complexes and $EuCl_3{\cdot}6H_2O$ with the similar Eu content were selected. At 24 h post-treatment, the cell suspension was placed in a 24-well 8.0 μm pore transwell chamber coated with or without Matrigel® Matrix (Corning) at a density of 5×10^5 cells. The medium in the upper chamber was serum-free, while the medium in the lower chamber contained 10% FBS and 1% PS as a source of attraction. After 24 h, non-migrated cells were removed using cotton swabs. The cells that migrated to the lower chamber were fixed with 4% formaldehyde and stained with 0.5% crystal violet. The assay was performed in triplicate, and three random views of each group were quantified using ImageJ software.

2.2.4 Cell pseudopodia morphology. The morphology of the K7M2 cells under different treatments was observed using a scanning electron microscope. K7M2 cells were seeded onto 10 mm glass slides in 12-well culture plates at a density of 5×10^4 cells per well for 24 h. The cells were then incubated with or without samples (*i.e.*, SPIO@BSA nano-complexes, Eu:SPIO@BSA nano-complexes, and $EuCl_3{\cdot}6H_2O$) for 24 h. The concentrations of SPIO@BSA, Eu:SPIO@BSA nano-complexes, and $EuCl_3{\cdot}6H_2O$ were 715 μg mL^{-1}, 530 μg mL^{-1}, and 18 μg mL^{-1}, respectively. The concentrations of SPIO@BSA and Eu:SPIO@BSA nano-complexes were selected for the similar Fe content. In addition, Eu:SPIO@BSA nano-complexes and $EuCl_3{\cdot}6H_2O$ with the similar Eu content were selected. After treatment for 24 h, the cells were scratched with a 1 mL pipette tip and allowed to migrate for 24 h. The next day, the cells were washed with PBS three times, fixed with 2.5% glutaraldehyde for 30 min, and again washed with PBS several times. The samples were dehydrated in a series of graded ethanol/water solutions (50%, 70%, 90%, 95%, and 100%, respectively, three times in each) and dried completely using a critical point dryer (CPD), (Tousimis, PVT-3D). Finally, the dehydrated cells were coated with platinum before observation using a scanning electron microscope.

2.3 Hemolysis assay

Hemolysis assays were performed to evaluate the hemolysis of Eu:SPIO@BSA nano-complexes and $EuCl_3{\cdot}6H_2O$ on red blood cells (RBCs) from mice. To obtain RBCs, fresh blood was collected from the mice and loaded into tubes containing (ethylenediaminetetraacetic acid) (EDTA; anticoagulant). RBCs were washed several times with 0.9% saline, collected by centrifugation at 3000 × *g* for 5 min, and diluted to a density of 3.33% (v/v). The Eu:SPIO@BSA nano-complexes and $EuCl_3{\cdot}6H_2O$ were added to the RBC suspension (5 : 1, v/v). In addition, 0.9% saline and distilled water were added to the RBCs suspension as negative and positive controls, respectively. After incubation for 2 h at 37 °C, the morphology of the RBCs was observed using a phase-contrast microscope (Nikon, TE2000-U).

2.4 *In vivo* study

Four-to six-week-old male nude mice (BALB/cAnN.Cg-Foxn1nu/CrlNarl) were purchased from the National Laboratory Animal

Center. All animals used in our experiments were treated and housed following a protocol approved by the Institutional Animal Care and Use Committee of the National Yang Ming Chiao Tung University (NYCU-IACUC 1100514).

2.4.1 Tumor accumulation. The effect of Eu:SPIO@BSA nano-complexes and $EuCl_3{\cdot}6H_2O$ on tumor accumulation was assessed through ICP-MS analysis. Mice were administered Eu:SPIO@BSA nano-complexes and $EuCl_3{\cdot}6H_2O$ *via* intravenous injection. Subsequently, a magnetic attraction was applied by placing a magnet (with a surface magnetic field strength of 5800 G) over the tumor for 1.5 h following the administration of the Eu:SPIO@BSA nano-complexes. After 1.5 and 36 h of injection, mice treated with Eu:SPIO@BSA nano-complexes and $EuCl_3{\cdot}6H_2O$ were sacrificed, and the Eu content within their tumors was quantified using ICP-MS.

2.4.2 Biochemical blood enzyme tests and histological examination. *In vivo* side effects associated with Eu:SPIO@BSA nano-complexes and $EuCl_3{\cdot}6H_2O$ treatments were evaluated by inspecting hepatic function *via* estimation of the serum levels of aspartate aminotransferase (AST) and alanine aminotransferase (ALT), and histological examination of hematoxylin and eosin (H&E) staining in nude mice after different treatments. Biochemical analyses were performed on blood samples obtained from nude mice after 24 h of the administration of Eu:SPIO@BSA nano-complexes and $EuCl_3{\cdot}6H_2O$. Concentrations of Eu:SPIO@BSA nano-complexes and $EuCl_3{\cdot}6H_2O$ were selected at the similar Eu content. Blood samples were collected and centrifuged at 3000 × *g* for 5 min to obtain serum. AST and ALT levels were measured using a Fuji DRI-Chem 4000i automated clinical chemistry analyzer. Normal ranges of AST, 50–215 U L^{-1}; ALT, 27–78 U L^{-1}.[22]

2.4.3 *In vivo* therapeutic efficacy. To observe metastasis from the proximal tibia to the lung, freshly trypsinized K7M2-Fluc cells (5×10^5) in a serum-free medium (10 μL) were intraosseously implanted into the right tibia of each mouse. *In vivo* imaging system (IVIS) spectrum (IVIS Luminar II, PerkinElmer) was used to monitor the tumor sites. After 2 weeks, the mice were assigned to three treatment groups (n = 3 per group): (1) control group, (2) Eu:SPIO@BSA nano-complexes group, and (3) $EuCl_3{\cdot}6H_2O$ group. The control group was intravenously administered saline. The treatment groups were intravenously injected with Eu:SPIO@BSA nano-complexes suspension (100 mg kg^{-1}) and $EuCl_3{\cdot}6H_2O$ solution (3.4 mg kg^{-1}), respectively. The mice were exposed to magnetic attraction by placing a magnet (surface magnetic field strength = 5800 G) on top of the tumor for 1.5 h after administering the Eu:SPIO@BSA nano-complexes suspension. The treatment was administered twice a week, and the luciferase signals of tumors and lung tissue were recorded using the IVIS spectrum on day 22, which was set as the endpoint. The animals were then sacrificed to collect lung tissues and tumors for histological examination by H&E staining. To adhere to the principles of 3R animal welfare and maintain the focus of our study on evaluating the efficacy of Eu:SPIO@BSA nano-complexes in *in vivo* experiments, we excluded animals receiving SPIO@BSA nano-complexes and animals without receiving magnetic attraction from the *in vivo* tests.

2.5 Statistical analysis

All *in vitro* experiments were repeated at least three times (n = 3, biologically independent experiments). Data are expressed as the mean ± standard deviation (SD) unless otherwise noted. Differences between groups were compared using analysis of variance (ANOVA) and multiple comparisons. A p-value of <0.05, was considered significant.

3. Results and discussions

3.1 Characterization of SPIO@BSA and Eu:SPIO@BSA nano-complexes

In this study, SPIO@BSA and Eu:SPIO@BSA nano-complexes were prepared following two-step procedures. In the first step, hydrophobic SPIO and Eu-doped SPIO (*i.e.*, Eu:SPIO) nanocrystals were synthesized following the pyrolysis method described in a previous study.[20] As shown in Fig. 1(A) and Fig. S1 (ESI†), XPS analysis of the SPIO and Eu:SPIO nanocrystals confirmed the successful doping of Eu ions into the SPIO nanocrystals. Moreover, SPIO and Eu:SPIO nanocrystals using XRD revealed diffraction angles at 30.4°, 35.5°, 43.2°, 57.1°, and 63.1°, assigned to the (220), (311), (400), (511), and (440) planes of Fe_3O_4 (JCPDS 26-1136), respectively, for all samples (Fig. 1(B)). This indicates that the crystal structure of SPIO were not altered by Eu doped. Further examination of the TEM images, as shown in Fig. 1(C) and (D), revealed homogenous SPIO and Eu:SPIO nanocrystals with an average particle size of 5 nm.

In the second step, SPIO and Eu:SPIO nanocrystals were incorporated into BSA through a self-assembly process to prepare hydrophilic SPIO@BSA and Eu:SPIO@BSA nano-complexes.[21] Fig. 1(E) and (F) depict the morphologies of SPIO@BSA and Eu:SPIO@BSA nano-complexes as revealed by TEM images. The magnetic properties of SPIO@BSA and Eu:SPIO@BSA nano-complexes were characterized using SQUID equipment (Fig. S2, ESI†). No hysteresis loops were observed in the *M–H* curves, implying that SPIO@BSA and Eu:SPIO@BSA nano-complexes exhibited superparamagnetic behavior. In addition, the saturated magnetization of Eu:SPIO@BSA nano-complexes was higher than that of SPIO@BSA nano-complexes owing to the Eu dopant.[23,24] These results demonstrated that the SPIO@BSA and Eu:SPIO@BSA nano-complexes were successfully synthesized.

To further analyze the amounts of Fe and Eu in the SPIO nanocrystals, Eu:SPIO nanocrystals, SPIO@BSA nano-complexes, and Eu:SPIO@BSA nano-complexes, ICP-MS analyses were conducted, as summarized in Table S1 (ESI†). In addition, the ratio of BSA in the SPIO@BSA and Eu:SPIO@BSA nano-complexes was calculated using TGA data. The results demonstrated that the BSA content in the SPIO@BSA and Eu:SPIO@BSA nano-complexes was approximately 52.52% and 52.57%, respectively (Fig. S3, ESI†). Notably, an increase in the thermal decomposition temperature of BSA was observed in both the SPIO@BSA and Eu:SPIO@BSA nano-complexes, suggesting potential interactions between BSA and either SPIO or Eu:SPIO nanocrystals within these formulations.

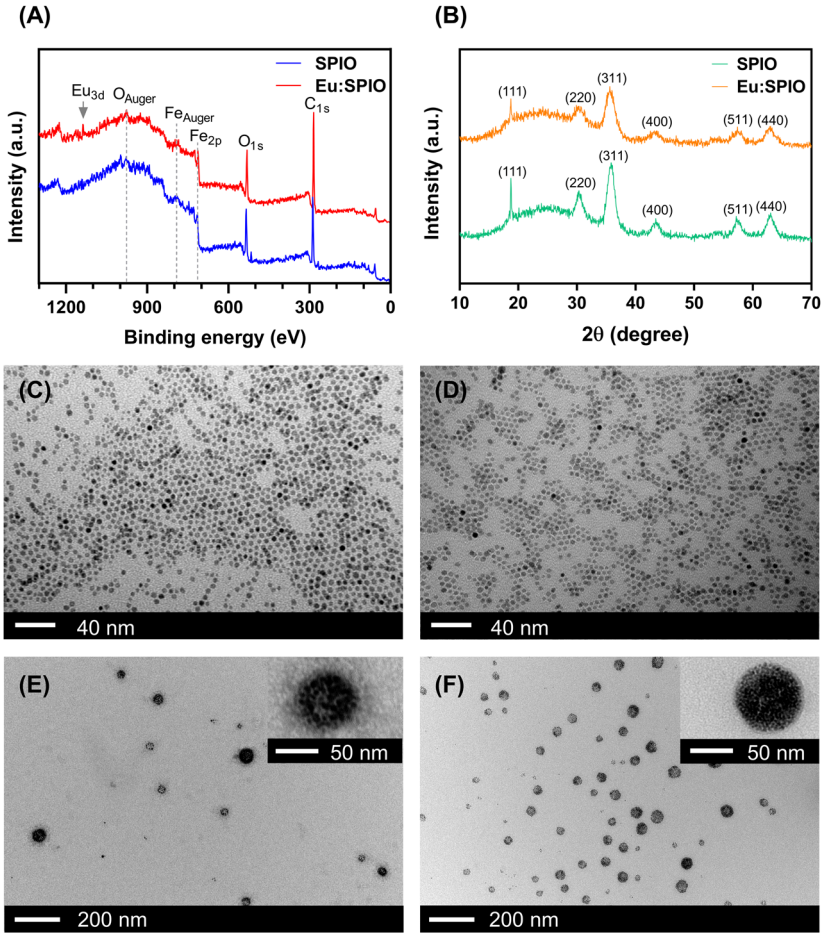

Fig. 1 Characterization of the SPIO nanocrystals, Eu-doped SPIO (*i.e.*, Eu:SPIO) nanocrystals, SPIO@BSA nano-complexes, and Eu:SPIO@BSA nano-complexes. Results of (A) survey X-ray photoelectron spectroscopy (XPS) spectra, and (B) X-ray diffraction (XRD) patterns of SPIO and Eu:SPIO nanocrystals. Transmission electron microscopy (TEM) images of (C) SPIO nanocrystals, (D) Eu:SPIO nanocrystals, (E) SPIO@BSA nano-complexes, and (F) Eu:SPIO@BSA nano-complexes.

3.2 *In vitro* biocompatibility, cellular internalization and *in vivo* tumor accumulation

SPIO and Eu:SPIO nanocrystals incorporated into BSA were used to enhance biocompatibility. In this study, nanovehicles (*i.e.*, SPIO@BSA and Eu:SPIO@BSA nano-complexes) were designed to be less toxic to avoid interfering with the assessment of metastasis inhibition caused by tumor suppression. As shown in Fig. S4 (ESI†), SPIO@BSA and Eu:SPIO@BSA nano-complexes demonstrated low toxicity to cells compared to $EuCl_3{\cdot}6H_2O$. Based on the toxicity assessment, the concentrations of SPIO@BSA nano-complexes, Eu:SPIO@BSA nano-complexes, and $EuCl_3{\cdot}6H_2O$ were selected as 715, 530, and 18 μg mL^{-1}, respectively, for the subsequent experiments. Under this condition, the concentrations of Fe in SPIO@BSA nano-complexes; Fe and Eu in Eu:SPIO@BSA nano-complexes; and Eu in $EuCl_3{\cdot}6H_2O$ were 25.45; 25.47 and 7.53; and 7.74 μg mL^{-1}, respectively.

Next, we investigated the effect of BSA on the cellular internalization of SPIO@BSA and Eu:SPIO@BSA nano-complexes in tumor cells. Confocal microscopy of MC3T3-E1 and K7M2 cells after 24 h incubation with fluorescent SPIO@BSA and Eu:SPIO@BSA nano-complexes (*i.e.*, SPIO@FITC-BSA and Eu:SPIO@FITC-BSA nano-complexes) showed the cellular internalization of SPIO@BSA and Eu:SPIO@BSA nano-complexes increased in K7M2 cells than that in MC3T3-E1 cells (Fig. 2(A) and Fig. S5, ESI†). These results could be attributed to the high binding affinity of BSA to tumor cells that overexpress albondin (*i.e.*, the 60-kDa albumin-binding protein) and SPARC (secreted protein acidic and rich in cysteine).[16,25] Overall, our results suggest that SPIO and Eu:SPIO nanocrystals incorporated into BSA enhance cellular internalization in K7M2 cells.

To further evaluate the potential of Eu:SPIO@BSA nano-complexes to enhance the accumulation of Eu content in tumors, we conducted *in vivo* experiments, comparing them with a $EuCl_3{\cdot}6H_2O$ group. As shown in Fig. 2(B), the Eu:SPIO@BSA nano-complexes exhibited a significant enhancement in the accumulation of Eu content within the tumor, in contrast to the $EuCl_3{\cdot}6H_2O$ group. This outcome can be attributed to the incorporation of Eu into SPIO and BSA, which facilitated precise delivery through magnetic attraction and BSA's active targeting. Overall, our findings suggest that Eu accumulation was achievable in both *in vitro* and *in vivo*

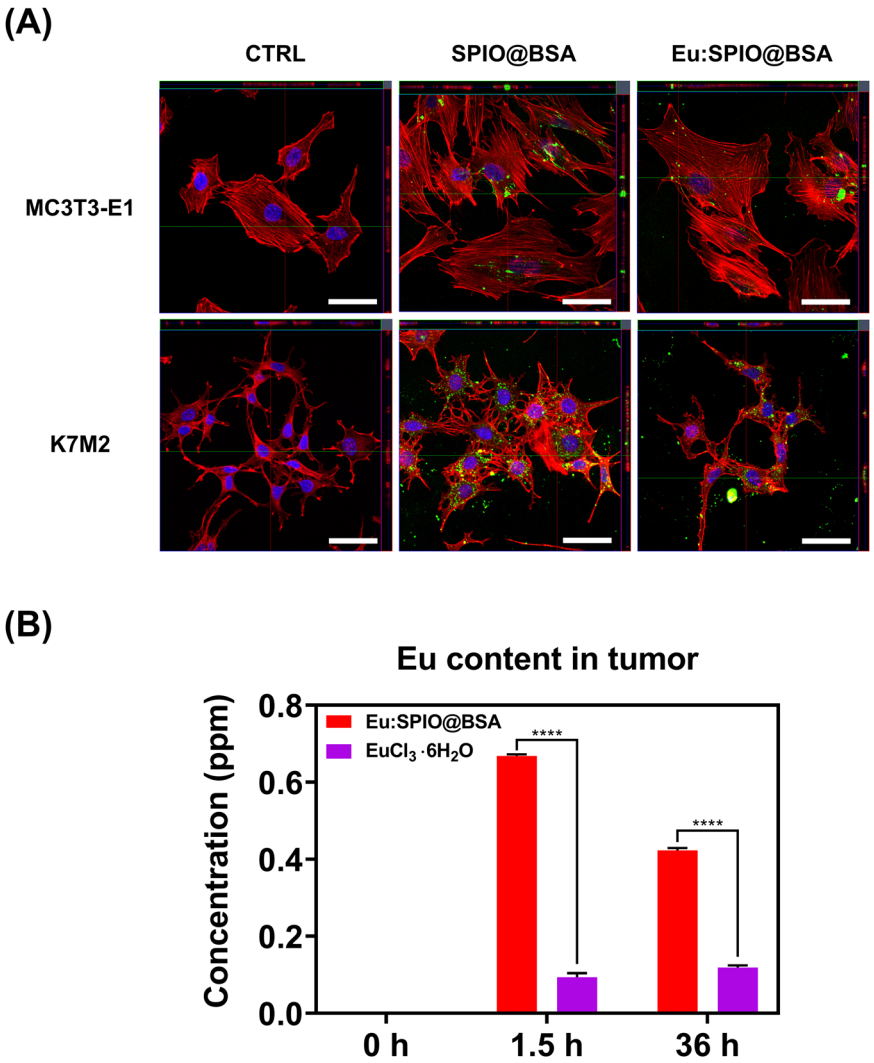

Fig. 2 *In vitro* cellular internalization and *in vivo* tumor accumulation of nano-complexes. Eu:SPIO@BSA nano-complexes demonstrated enhanced Eu accumulation through both *in vitro* cellular internalization and *in vivo* tumor accumulation. (A) Confocal microscopy images of cellular internalization of fluorescent SPIO@BSA and Eu:SPIO@BSA nano-complexes (*i.e.*, SPIO@FITC-BSA and Eu:SPIO@FITC-BSA) in K7M2 and MC3T3-E1. *In vitro*, the cells were incubated with fluorescent SPIO@BSA (715 μg mL^{-1}) and Eu:SPIO@BSA nano-complexes (530 μg mL^{-1}) for 24 h, and the cellular internalization of fluorescent nano-complexes was examined using a confocal laser scanning microscope (CLSM). Cell nuclei and actin were stained with DAPI (blue) and Alexa Fluor™ 568 Phalloidin (red), respectively. Fluorescent SPIO@BSA and Eu:SPIO@BSA nano-complexes are visible in green color. Scale bar = 50 μm. CTRL represents a control group that did not receive any treatments. (B) Tumor accumulation of Eu:SPIO@BSA nano-complexes and $EuCl_3{\cdot}6H_2O$ determined using ICP-MS analysis. *In vivo*, mice were treated with Eu:SPIO@BSA nano-complexes and $EuCl_3{\cdot}6H_2O$ and sacrificed after 1.5 and 36 h post the injection. Eu:SPIO@BSA nano-complexes and $EuCl_3{\cdot}6H_2O$ were selected at the similar Eu content. The results of (B) are expressed as mean ± standard deviation (SD) of n = 3 biologically independent samples. Statistical analysis was performed using two-way ANOVA (****$p < 0.0001$).

conditions. These results underscore the potential of Eu:SPIO@BSA nano-complexes as a promising platform for enhancing localized drug delivery in cancer therapy.

3.3 Effect of Eu:SPIO@BSA nano-complexes on migration and invasion inhibition to K7M2 cells

To compare the migration-inhibiting and invasion-inhibiting effect of SPIO@BSA nano-complexes, Eu:SPIO@BSA nano-complexes, and $EuCl_3{\cdot}6H_2O$ on K7M2 cells, wound healing and transwell assays were performed. As shown in Fig. 3, a slight migration-inhibiting effect was observed in the SPIO@BSA nano-complexes group. In addition, Eu:SPIO@BSA nano-complexes and $EuCl_3{\cdot}6H_2O$ groups demonstrated a migration-inhibiting effect. Similar results were observed in transwell assays, in which the cell migration and invasion abilities were significantly decreased by Eu:SPIO@BSA nano-complexes and $EuCl_3{\cdot}6H_2O$ compared to those by the control and SPIO@BSA nano-complexes (Fig. 4). A previous study showed that lanthanides such as Eu^{3+} ions competitively combine with the MT1-MMP receptor, which decreases cell migration.[12,26] In our study, $EuCl_3{\cdot}6H_2O$ significantly inhibited the migration and invasion of K7M2 (Fig. 3 and 4). Moreover, the migration-inhibiting effect of Eu ions remained evident when Eu ions were doped into SPIO and incorporated into BSA (Eu:SPIO@BSA nano-complexes). This is supported by the

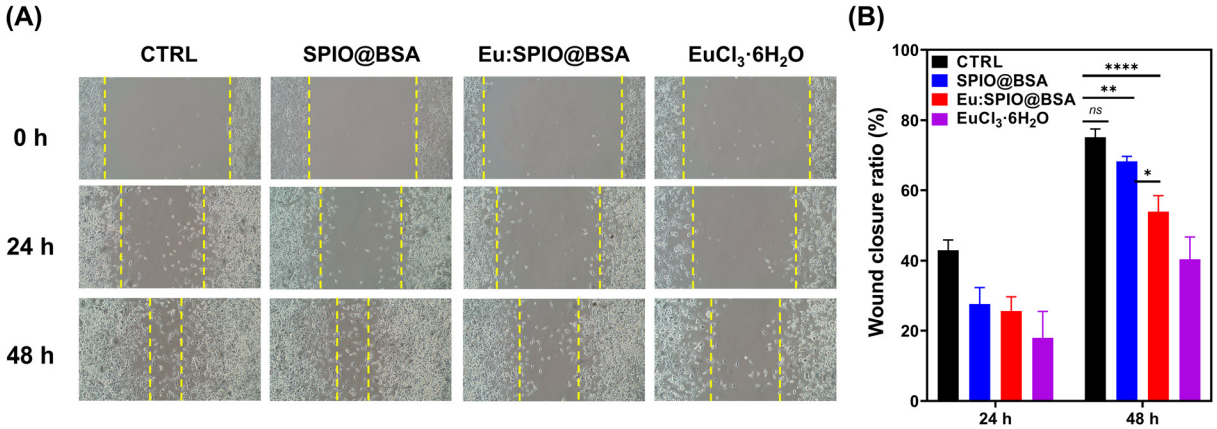

Fig. 3 Effect of SPIO@BSA nano-complexes, Eu:SPIO@BSA nano-complexes, and $EuCl_3{\cdot}6H_2O$ on the migration of K7M2 cells determined using scratch-wound healing assay. (A) Representative microscope images. (B) Quantification of wound closure ratio. The migration ability of K7M2 cells were significantly decreased by Eu:SPIO@BSA nano-complexes. K7M2 cells were treated with SPIO@BSA nano-complexes (715 μg mL^{-1}), Eu:SPIO@BSA nano-complexes (530 μg mL^{-1}) and $EuCl_3{\cdot}6H_2O$ (18 μg mL^{-1}) for 24 h. Afterward, cells were scratched using 1 mL pipette tips, and the cell migration was observed using a phase-contrast microscope. Quantitative results of the wound closure ratio were analyzed according to the initial scraped area using ImageJ software. The concentrations of SPIO@BSA and Eu:SPIO@BSA nano-complexes were selected at the similar Fe content. The concentrations of Eu:SPIO@BSA nano-complexes and $EuCl_3{\cdot}6H_2O$ were selected at the similar Eu content. The results of (B) are expressed as mean ± standard deviation (SD) of n = 3 biologically independent samples. Statistical analysis was performed using two-way ANOVA (*$p < 0.05$, **$p < 0.01$ and ****$p < 0.0001$). CTRL represents a control group that did not receive any treatments.

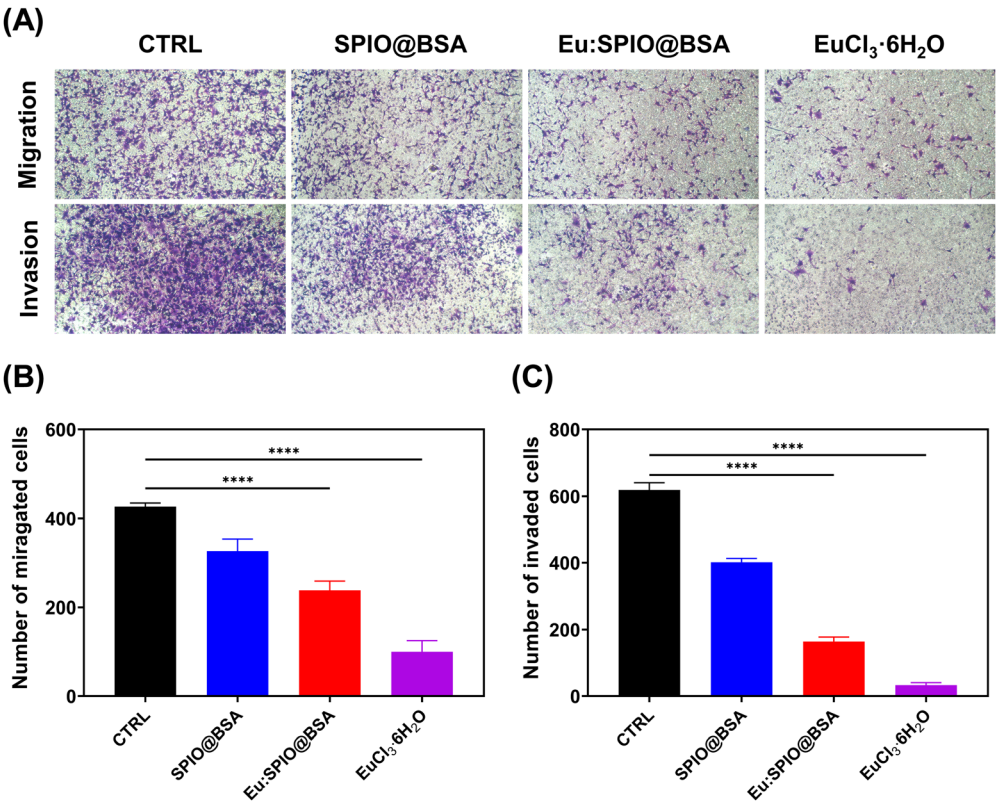

Fig. 4 Effect of SPIO@BSA, Eu:SPIO@BSA nano-complexes, and $EuCl_3{\cdot}6H_2O$ on migration and invasion capacity of K7M2 cells examined using transwell chamber assays. (A) Representative microscope images. Quantification of (B) migrated and (C) invaded cells on the bottom of the transwell chamber. The migration and invasion ability of K7M2 cells were significantly decreased by Eu:SPIO@BSA nano-complexes. K7M2 cells were incubated with SPIO@BSA nano-complexes (715 μg mL^{-1}), Eu:SPIO@BSA nano-complexes (530 μg mL^{-1}), and $EuCl_3{\cdot}6H_2O$ (18 μg mL^{-1}) for 24 h. Afterward, cells were collected and placed in the upper chamber for 24 h. The concentrations of SPIO@BSA and Eu:SPIO@BSA nano-complexes were selected at the similar Fe content. In addition, the concentrations of Eu:SPIO@BSA nano-complexes and $EuCl_3{\cdot}6H_2O$ were selected at the similar Eu content. The number of migrated and invaded K7M2 cells was counted using ImageJ software. The results are expressed as mean ± SD of n = 3 biologically independent samples. Statistical analysis was performed using one-way ANOVA (****$p < 0.0001$).

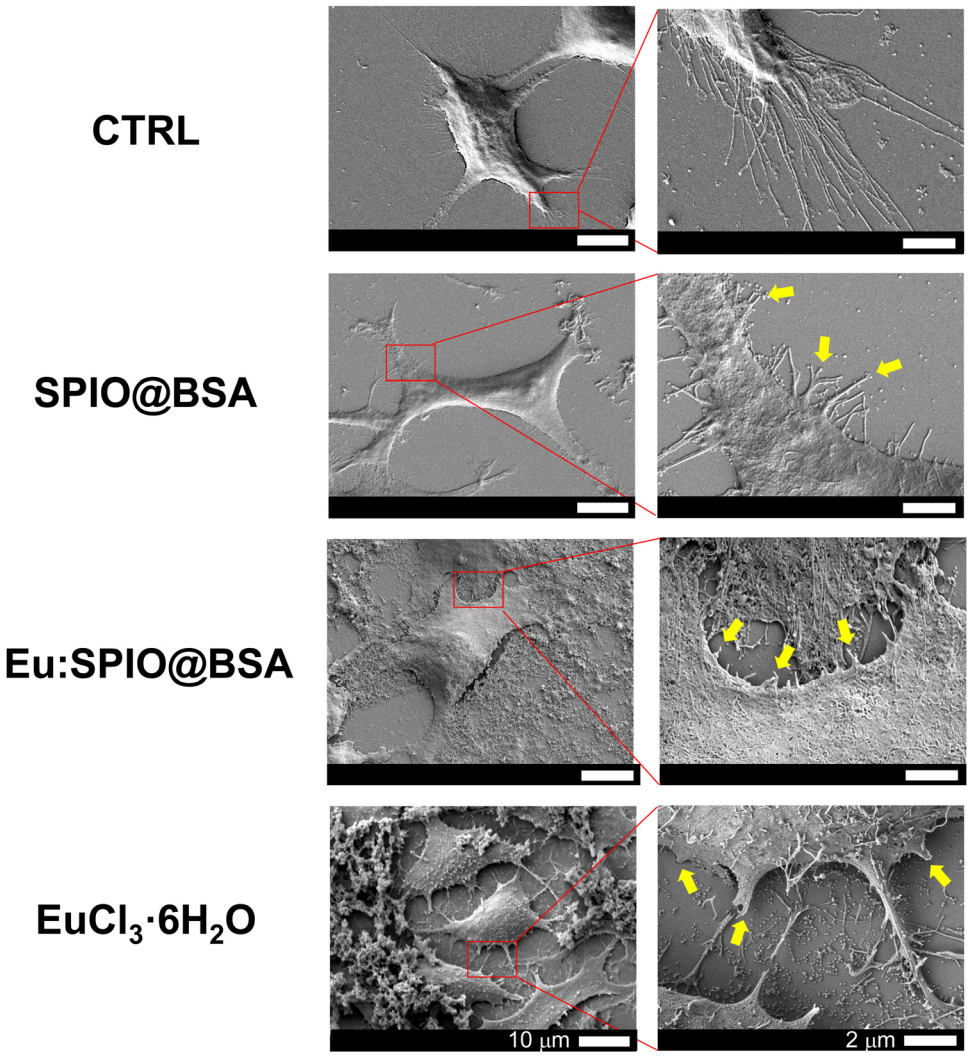

Fig. 5 Morphologies of K7M2 cells treated with SPIO@BSA nano-complexes, Eu:SPIO@BSA nano-complexes, and $EuCl_3{\cdot}6H_2O$ observed using scanning electron microscopy (SEM) images at 24 h post-treatment. The morphologies of cell pseudopodia were altered and became shorter following treatment with Eu:SPIO@BSA nano-complexes. The concentrations of SPIO@BSA (715 μg mL^{-1}) and Eu:SPIO@BSA nano-complexes (530 μg mL^{-1}) were selected at the similar Fe content. In addition, concentrations of Eu:SPIO@BSA nano-complexes and $EuCl_3{\cdot}6H_2O$ were selected at the similar Eu content. Yellow arrows indicate protrusion, like the shape of lamellipodia and filopodia changing.

results shown in Fig. S6A (ESI†), in which Eu ions significantly decreased the expression of matrix metalloproteinase-2 (MMP-2) protein (*i.e.*, a matrix metalloproteinase associated with the degradation of the extracellular matrix before metastasis).[27,28] In addition, the SPIO@BSA nano-complexes exerted a slight migration-inhibiting effect (Fig. 3 and 4), possibly due to the interaction between Fe-containing nano-complexes and cell migration proteins on the cell migration pathway.[29,30]

To confirm the effect of nanovehicles on migration and invasion, the effects of SPIO@BSA nano-complexes, Eu:SPIO@BSA nano-complexes, and $EuCl_3{\cdot}6H_2O$ on morphologies of K7M2 cells were investigated. As shown in Fig. 5, the extended cell pseudopodia were observed in the CTRL group. However, the morphologies of cell pseudopodia were altered and became shorter following treatment with Eu:SPIO@BSA nano-complexes and $EuCl_3{\cdot}6H_2O$. This could be attributed to the effect of the nano-scale particles or transition elements on cytoskeleton modeling and cell migration.[31–33] Furthermore, these results were further supported by the increased expression of vinculin, an adhesion-related protein in K7M2 cells treated with Eu:SPIO@BSA nano-complexes and $EuCl_3{\cdot}6H_2O$ (Fig. S6B, ESI†). Taken together, our results support the hypothesis that Eu:SPIO@BSA nano-complexes affect migration and invasion inhibition.

3.4 Hemocompatibility of Eu:SPIO@BSA nano-complexes

In *in vitro* studies, the migration-inhibiting effects of SPIO@BSA nano-complexes were less pronounced than those of Eu:SPIO@BSA nano-complexes and $EuCl_3{\cdot}6H_2O$. Hence, given our focus on investigating and comparing the hemocompatibility and *in vivo* effects of Eu-containing formulations, particularly Eu:SPIO@BSA nano-complexes and $EuCl_3{\cdot}6H_2O$, we

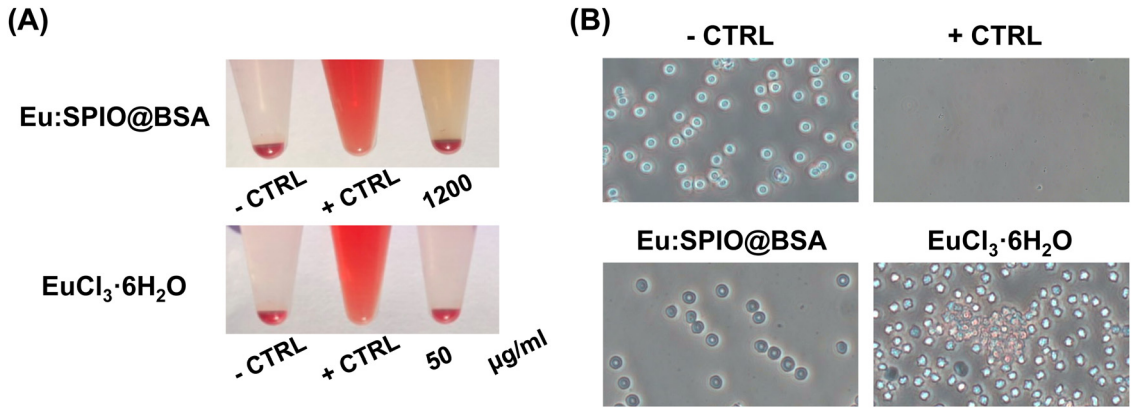

Fig. 6 Hemolytic effects of Eu:SPIO@BSA nano-complexes and $EuCl_3{\cdot}6H_2O$. (A) Hemolysis images captured using digital photography; (B) optical microscopy images depicting morphologies of red blood cells (RBCs) following treatment with Eu:SPIO@BSA nano-complexes and $EuCl_3{\cdot}6H_2O$. Hemagglutination of red blood cells was observed in the $EuCl_3{\cdot}6H_2O$ group, whereas no hemolysis was observed in the Eu:SPIO@BSA nano-complexes group. RBCs were treated with Eu:SPIO@BSA nano-complexes and $EuCl_3{\cdot}6H_2O$ for 2 h before the observation. Negative control (−CTRL) was treated with phosphate-buffered solution, and positive control (+CTRL) was treated with double-distilled H_2O.

chose to concentrate our efforts on these two formulations in subsequent experiments.

To evaluate the hemocompatibility of Eu:SPIO@BSA nano-complexes and $EuCl_3{\cdot}6H_2O$, RBCs hemolysis experiments were performed. The concentrations of Eu:SPIO@BSA nano-complexes and $EuCl_3{\cdot}6H_2O$ utilized in the hemolysis experiments were derived from the estimation of the concentrations of the active agents in the blood of animals during *in vivo* studies. As shown in Fig. 6(A), no hemolysis was observed in Eu:SPIO@BSA nano-complexes and $EuCl_3{\cdot}6H_2O$ group. However, RBCs became hemagglutinated in the $EuCl_3{\cdot}6H_2O$ group (Fig. 6(B)). This phenomenon could be attributed to an interaction of lanthanide elements with surface membrane proteins of RBCs, probably inducing alterations in cellular configuration and morphology.[34,35]

3.5 *In vivo* therapeutic efficacy of Eu:SPIO@BSA nano-complexes

Based on previous studies on the toxicity of iron oxide and lanthanides,[36–38] as well as our preliminary investigations, we have determined that the usable dosage of Eu:SPIO@BSA nano-complexes can be increased to 100 mg kg^{-1}. Thus, all subsequent *in vivo* experiments will be conducted using this concentration, while also maintaining a similar Eu content in the $EuCl_3{\cdot}6H_2O$ group. As shown in Fig. 7, the effects of Eu:SPIO@BSA nano-complexes and $EuCl_3{\cdot}6H_2O$ on hepatic damage revealed no symptoms of liver damage in the Eu:SPIO@BSA nano-complexes treated group. However, AST and ALT levels significantly increased in $EuCl_3{\cdot}6H_2O$ group (Fig. 7(A)). Moreover, abnormal liver cells were observed in histological images of $EuCl_3{\cdot}6H_2O$-treated mice (Fig. 7(B)). Furthermore, Eu:SPIO@BSA nano-complexes demonstrated higher accumulation in the tumors than $EuCl_3{\cdot}6H_2O$ (Fig. 2(B)). These results indicate that Eu-doped SPIO incorporated into BSA vehicles demonstrates lower toxicity and higher tumor accumulation than $EuCl_3{\cdot}6H_2O$.

Further investigation of *in vivo* therapeutic efficacy of Eu:SPIO@BSA nano-complexes and $EuCl_3{\cdot}6H_2O$ is shown in

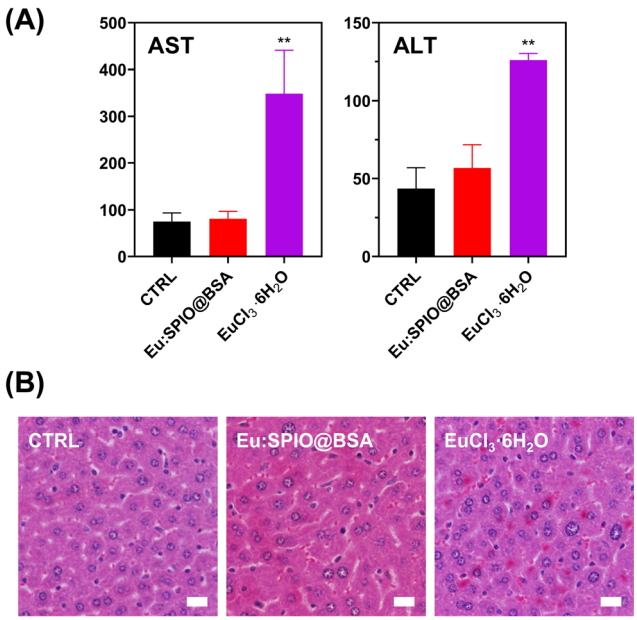

Fig. 7 Hepatic toxicity of Eu:SPIO@BSA nano-complexes and $EuCl_3{\cdot}6H_2O$ determined using (A) biochemical blood enzyme tests and (B) histological examinations of hematoxylin and eosin (H&E) staining. No symptoms of liver damage in the Eu:SPIO@BSA nano-complexes treated group; however, AST and ALT levels significantly increased in $EuCl_3{\cdot}6H_2O$ group. Mice were treated with Eu:SPIO@BSA nano-complexes (100 mg kg^{-1}) and $EuCl_3{\cdot}6H_2O$ (3.4 mg kg^{-1}). At 24 h post-treatment, the hepatic function was evaluated by estimating the levels of the aspartate aminotransferase (AST) and alanine aminotransferase (ALT). The results are expressed as mean ± SD, n = 3 biologically independent samples. Statistical analysis was performed using one-way ANOVA compared with the control group (**$p < 0.01$). Normal ranges of AST: 50–215 U L^{-1}, ALT: 27–78 U L^{-1}. Scale bar = 20 μm.

Fig. 8. K7M2 cells expressing luciferase were injected into the tibia of mice. After 14 days, mice were treated with Eu:SPIO@BSA nano-complexes and $EuCl_3{\cdot}6H_2O$. Primary tumor size and distant lung metastasis were evaluated using the IVIS spectrum

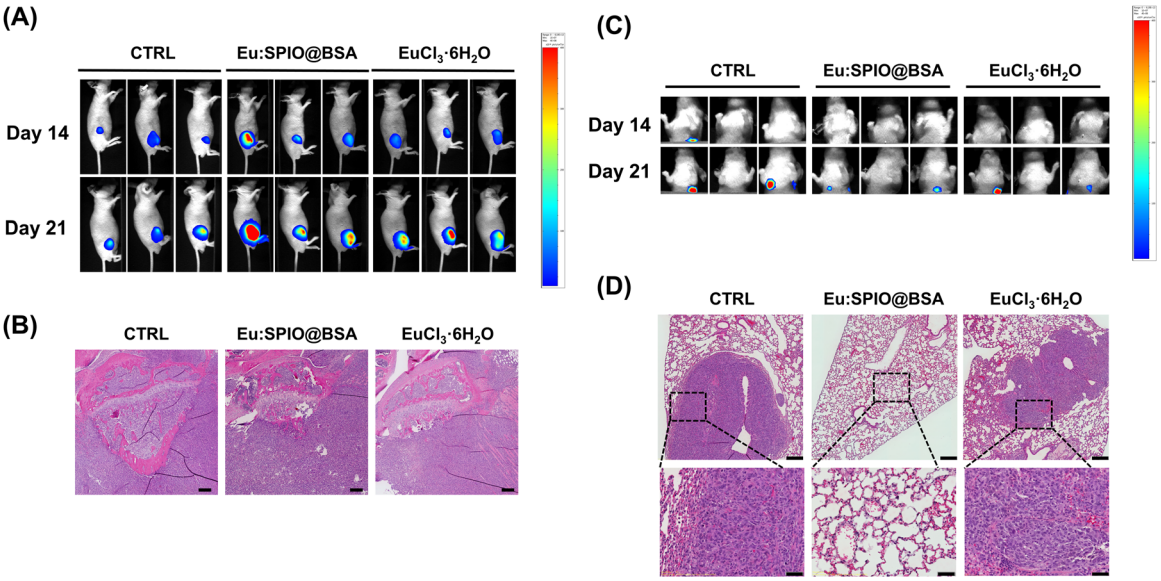

Fig. 8 *In vivo* therapeutic efficacy of Eu:SPIO@BSA nano-complexes, and $EuCl_3{\cdot}6H_2O$ on the (A) and (B) growth and (C) and (D) lung metastasis of osteosarcoma assessed using *in vivo* imaging system (IVIS) and histological examinations of H&E staining. The growth of the primary tumor was not suppressed; however, distant lung metastasis was reduced by the Eu:SPIO@BSA nano-complexes. The CTRL group was not treated with any nanovehicles or compounds. The concentrations of Eu:SPIO@BSA nano-complexes (100 mg kg^{-1}) and $EuCl_3{\cdot}6H_2O$ (3.4 mg kg^{-1}) were selected at the similar Eu content. The treatments were performed twice a week. Scale bar = (B) 200 μm, (D, top) 200 μm, and (D, down) 50 μm.

and histological images. To avoid interference with the assessment of metastasis inhibition caused by tumor suppression, the vehicles in this study were designed to be less toxic to tumor cells. In our preliminary experiments, variations in the speed of tumor metastasis were observed among mice, suggesting potential individual differences. Therefore, in this study, we focused on assessing the therapeutic effects of Eu:SPIO@BSA specifically in mice that had already exhibited metastasis. As shown in Fig. 8(A) and (B), growth-inhibiting effect on the primary tumor was not observed in any of the groups. However, even if the growth of the primary tumor was not suppressed, distant lung metastasis was reduced by the Eu:SPIO@BSA nano-complexes (Fig. 8(C) and (D)). This is supported by the migration-inhibiting effect of Eu:SPIO@BSA nano-complexes *in vitro* (Fig. 3–5). Although $EuCl_3{\cdot}6H_2O$ demonstrated the highest migration-inhibiting effect *in vitro*, it did not demonstrate a similar effect *in vivo* (Fig. 8(C), (D) and Fig. S7, ESI†). This could be attributed to the fact that the lower concentration of Eu in the tumors obtained from mice treated with $EuCl_3{\cdot}6H_2O$ (Fig. 2(B)). This result supports the idea that Eu incorporated into the SPIO matrix can achieve higher tumor accumulation through the intravenous delivery under magnetic attraction.

In the metastasis cascade, antitumor migration and invasion are the key steps for preventing tumor metastasis. Although $EuCl_3{\cdot}6H_2O$ demonstrates promising migrastatic and MMPIs potential in *in vitro* experiments, its lack of biocompatibility and tumor accumulation functionalities hinders its practical application. This limitation can be effectively addressed through the utilization of Eu:SPIO@BSA hybrid nano-complexes. In this study, we successfully prepared Eu:SPIO@BSA nano-complexes, which exhibited a significant reduction in distant tumor metastasis compared to $EuCl_3{\cdot}6H_2O$ groups. This study primarily focused on elucidating the influence of Eu:SPIO@BSA nano-complexes on cell migration and cytoskeleton. However, the detailed mechanisms underlying the effects of Eu required further exploration. The utilization of Eu:SPIO@BSA nano-complexes as a magnetism-enhanced targeted delivery system holds significant potential in enhancing the precision and effectiveness of anti-metastatic therapies. The main objective of this study was to develop a strategy focused on inhibiting metastasis, rather than eliminating the primary tumor. For the treatment of the primary tumor, this strategy could be combined with established methods such as radiotherapy and chemotherapy to enhance overall effectiveness in addressing both metastasis and localized tumor growth in the future. Further validation, including biodistribution, pharmacokinetic, and long-term toxicity analyses, is inherently complex and can be significantly affected by variables such as particle size and drug dosage. These comprehensive studies are suitable for detailed exploration in a separate publication. In summary, this innovative approach has the potential to complement and be combined with standard cancer treatments, introducing a paradigm shift in the field of cancer treatment.

4. Conclusions

In the present study, we developed a hybrid nano-complex—Eu:SPIO@BSA—to prevent lung metastasis in osteosarcoma. Eu:SPIO@BSA nano-complexes inhibited migration and invasion *in vitro*. In addition, *in vivo* studies indicated that distant

lung metastasis was inhibited by the magnetism-enhanced targeted delivery of Eu:SPIO@BSA nano-complexes through I.V. injection. Compared with $EuCl_3 \cdot 6H_2O$, the strategy proposed in the present study demonstrated higher hemocompatibility, lower liver toxicity and higher metastasis-inhibiting efficacy *in vivo*. The results of this study demonstrate that Eu:SPIO@BSA nano-complexes are potential candidates for improving the therapeutic efficacy of metastasis prevention.

Author contributions

Yu-Chi Wang: conceptualization, data curation, formal analysis, project administration, supervision, visualization, writing – original draft and writing – review & editing; Fu-I. Tung: conceptualization, methodology, mentorship, funding acquisition and resources; Zheng-Ying Sung: conceptualization, data curation, formal analysis, investigation, methodology and validation; Mei-Hsiu Chen: resources; Ming-Hong Chen: resources; Tse-Ying Liu: conceptualization, funding acquisition, investigation, methodology, supervision and writing – review & editing.

Conflicts of interest

There are no conflicts to declare.

Acknowledgements

We are grateful to the Ministry of Science and Technology (MOST 111-2221-E-A49-051-MY2, MOST 111-2811-E-A49A-007-MY2, MOST 111-2314-B-038-094, MOST 110-2622-E-A49A-504, MOST 109-2221-E-010-020-MY2, and MOST 108-2314-B-010-035-MY3), the Far Eastern Memorial Hospital (FEMH-2024-C-013, FEMH-2024-C-057 and FEMH-2023-C-081), and the Department of Health, Taipei City Government (11201-62-004, and 11101-62-009) for financial support.

Notes and references

1 C. N. Qian, Y. Mei and J. Zhang, *Chin. J. Cancer*, 2017, **36**, 38.
2 A. W. Lambert, D. R. Pattabiraman and R. A. Weinberg, *Cell*, 2017, **168**, 670–691.
3 X. Guan, *Acta Pharm. Sin. B*, 2015, **5**, 402–418.
4 A. A. Schegoleva, A. A. Khozyainova, T. S. Gerashchenko, L. D. Zhuikova and E. V. Denisov, *Clin. Exp. Metastasis*, 2022, **39**, 505–519.
5 G. L. Farfalli, J. I. Albergo, P. A. Lobos, D. E. Smith, P. D. Streitenberger, M. G. Pallotta Rodríguez and L. A. Aponte-Tinao, *Medicina*, 2015, **75**, 87–90.
6 E. Lavit, M. Aldea, S. Piperno-Neumann, N. Firmin, A. Italiano, N. Isambert, J.-E. Kurtz, C. Delcambre, V. Lebrun, P. Soibinet-Oudot, C. Chevreau, E. Bompas, C. Le Maignan, P. Boudou-Rouquette, A. Le Cesne, J. Mancini, J.-Y. Blay and F. Duffaud, *Int. J. Cancer*, 2022, **150**, 645–653.
7 L. A. Hapach, J. A. Mosier, W. Wang and C. A. Reinhart-King, *npj Precis. Oncol.*, 2019, **3**, 20.
8 J. Solomon, M. Raškova, D. Rösel, J. Brábek and H. Gil-Henn, *Cells*, 2021, **10**, 1845.
9 R. E. Vandenbroucke and C. Libert, *Nat. Rev. Drug Discovery*, 2014, **13**, 904–927.
10 H. Chen, S. Liu, L. Miao, L. Yu, Y. Wang and F. Guo, *J. Rare Earths*, 2013, **31**, 94–100.
11 P. Wang, X.-M. Zou, J. Huang, T.-L. Zhang and K. Wang, *Cell Biol. Int.*, 2011, **35**, 1159–1167.
12 Y. Wang, Y. Wang, S. An, J. Zhang, Y. Han, J. Xu, F. Yu, D. Yu and X. Fang, *RSC Adv.*, 2018, **8**, 14347–14354.
13 Y.-C. Wang, S.-h Tsai, M.-H. Chen, F.-Y. Hsieh, Y.-C. Chang, F.-I. Tung and T.-Y. Liu, *ACS Appl. Mater. Interfaces*, 2022, **14**, 5586–5597.
14 H. P. Chen, F. I. Tung, M. H. Chen and T. Y. Liu, *J. Controlled Release*, 2016, **226**, 182–192.
15 P. Kumar, S. Agnihotri and I. Roy, *Int. J. Nanomed.*, 2018, **13**, 43–46.
16 P. Zhao, Y. Wang, A. Wu, Y. Rao and Y. Huang, *ChemBioChem*, 2018, **19**, 1796–1805.
17 S. Xu, J. Wang, Y. Wei, H. Zhao, T. Tao, H. Wang, Z. Wang, J. Du, H. Wang, J. Qian, K. Ma and J. Wang, *ACS Appl. Mater. Interfaces*, 2020, **12**, 56701–56711.
18 S. Chen, Q. Liang, E. Liu, Z. Yu, L. Sun, J. Ye, M.-C. Shin, J. Wang and H. He, *J. Mater. Chem. B*, 2017, **5**, 4060–4072.
19 A. Gandalovičová, D. Rosel, M. Fernandes, P. Veselý, P. Heneberg, V. Čermák, L. Petruželka, S. Kumar, V. Sanz-Moreno and J. Brábek, *Trends Cancer*, 2017, **3**, 391–406.
20 J. C. Park, S. Yeo, M. Kim, G. T. Lee and J. H. Seo, *Mater. Lett.*, 2016, **181**, 272–277.
21 F. Galisteo-González and J. A. Molina-Bolívar, *Colloids Surf., B*, 2014, **123**, 286–292.
22 Y.-P. Sher and M.-C. Hung, *Bio-Protoc.*, 2013, **3**, e931.
23 M. H. N. Assadi, J. J. Gutiérrez Moreno, D. A. H. Hanaor and H. Katayama-Yoshida, *Phys. Chem. Chem. Phys.*, 2021, **23**, 20129–20137.
24 J. M. Millward, A. Ariza de Schellenberger, D. Berndt, L. Hanke-Vela, E. Schellenberger, S. Waiczies, M. Taupitz, Y. Kobayashi, S. Wagner and C. Infante-Duarte, *Neuroscience*, 2019, **403**, 136–144.
25 C. C. Fleischer and C. K. Payne, *Acc. Chem. Res.*, 2014, **47**, 2651–2659.
26 Y. Song, J. Jin, J. Li, R. He, M. Zhang, Y. Chang, K. Chen, Y. Wang, B. Sun and G. Xing, *J. Nanosci. Nanotechnol.*, 2014, **14**, 4022–4028.
27 C. Ogier, A. Bernard, A. M. Chollet, T. Le Diguardher, S. Hanessian, G. Charton, M. Khrestchatisky and S. Rivera, *Glia*, 2006, **54**, 272–284.
28 K. Sanka, R. Maddala, D. L. Epstein and P. V. Rao, *Invest. Ophthalmol. Visual Sci.*, 2007, **48**, 2105–2114.
29 V. Mulens-Arias, J. M. Rojas, S. Pérez-Yagüe, P. Morales Mdel and D. F. Barber, *J. Controlled Release*, 2015, **216**, 78–92.
30 H. Wen, Y. Qin, W. Zhong, C. Li, X. Liu and Y. Shen, *Enzyme Microb. Technol.*, 2016, **92**, 9–17.
31 C. Y. Tay, P. Cai, M. I. Setyawati, W. Fang, L. P. Tan, C. H. L. Hong, X. Chen and D. T. Leong, *Nano Lett.*, 2014, **14**, 83–88.

32 M. R. K. Ali, Y. Wu, Y. Tang, H. Xiao, K. Chen, T. Han, N. Fang, R. Wu and M. A. El-Sayed, *Proc. Natl. Acad. Sci. U. S. A.*, 2017, **114**, E5655–E5663.
33 M. R. K. Ali, Y. Wu, Y. Tang, H. Xiao, K. Chen, T. Han, N. Fang, R. Wu and M. A. El-Sayed, *Proc. Natl. Acad. Sci. U. S. A.*, 2017, **114**, E5655–E5663.
34 T. Alexy, O. K. Baskurt, N. Nemeth, M. Uyuklu, R. B. Wenby and H. J. Meiselman, *Biorheology*, 2011, **48**, 173–183.
35 Y.-J. Zheng, J. Lu, L. Ding, H.-T. Chen and D.-Q. Zhao, *Chem. Lett.*, 2001, 158–159.
36 N. Malhotra, J.-S. Lee, R. A. D. Liman, J. M. S. Ruallo, O. B. Villaflores, T.-R. Ger and C.-D. Hsiao, *Molecules*, 2020, **25**, 3159.
37 Y. Ogawa, S. Suzuki, K. Naito, M. Saito, E. Kamata, A. Hirose, A. Ono, T. Kaneko, M. Chiba and Y. Inaba, *J. Environ. Pathol. Toxicol.*, 1995, **14**, 1–9.
38 T. J. Haley, N. Komesu, G. Colvin, L. Koste and H. C. Upham, *J. Pharm. Sci.*, 1965, **54**, 643–645.